Journal of Alloys and Compounds 505 (2010) 743–749

Contents lists available at ScienceDirect

Journal of Alloys and Compounds

journal homepage: www.elsevier.com/locate/jallcom

Electrical and dielectric properties of co-precipitated nanocrystalline tin oxide

A.R. Babar[a], S.S. Shinde[a], A.V. Moholkar[b,c], K.Y. Rajpure[a,*]

[a] Electrochemical Materials Laboratory, Department of Physics, Shivaji University, Kolhapur 416004, M.S., India
[b] Department of Physics, Gopal Krishna Gokhale College, Kolhapur 416012, M.S., India
[c] Department of Materials Science and Engineering, Chonnam National University, 300 Yongbong-Dong, Buk-Gu, Gwangju 500-757, South Korea

ARTICLE INFO

Article history:
Received 22 December 2009
Received in revised form 16 June 2010
Accepted 22 June 2010
Available online 1 July 2010

Keywords:
Chemical co-precipitation
Tin oxide
XRD
Crystallite size
FTIR
SEM
Electrical and dielectric properties
XPS studies

ABSTRACT

Nanocrystalline tin oxide (SnO_2) powders were synthesized by chemical co-precipitation method using stannic chloride pentahydrate ($SnCl_4{\cdot}5H_2O$) precursor in aqueous medium. The influence of sintering temperatures on the crystalline structure, morphological, electrical, dielectric and XPS properties has been studied. X-ray diffraction study reveals that sintered powder which exhibits tetragonal crystal structure and both crystallinity as well as crystal size increase with increase in temperature. The nature of species of various absorption bonds viz. Sn–O, O–Sn–O and O–H involved in sintered SnO_2 samples has been studied using FTIR technique. The morphological studies reveal randomly arranged grains with compact nature and grain size increases with sintering temperature. Measurements of electrical properties show relatively lower resistivity ($\approx 10^2$–$10^3\ \Omega$ cm) and higher dielectric constant at 400 °C than other sintering temperatures. The compositional analysis and electronic behavior of SnO_2 nanoparticles is studied using X-ray photoelectron spectroscopy. The symmetric spin orbit splitting of Sn $3d_{5/2}$ ground state and Sn $3d_{3/2}$ excited states is observed with sintering temperature while O 1s is recognized with O_2^- state.

1. Introduction

The nano-material forms the building blocks for new bottom-up approaches due to their intrinsic size dependent properties and resulting applications. Renewed interest has been developed in tin oxide (SnO_2) due to its mechanical and chemical stability, environmental and good thermal properties [1,2]. In the bulk form, SnO_2 has a tetragonal structure ($a = b = 4.737$ Å and $c = 3.186$ Å), similar to the rutile structure with the wide energy gap $E_g = 3.67$ eV, an insulator and becomes n-type semiconductor when deposited in thin film form [3]. It plays an important role as transparent conductive oxide (TCO) material with remarkable photoelectrical properties such as solar battery, intelligent window, transparent electrode, electrochemical supercapacitors and low-e windows [4–7], etc. Especially, SnO_2 nanoparticles have been intensively studied for gas sensing [8,9] applications not only because of their relatively low operating temperature, but also due to dual purpose of detecting reducing and oxidizing gases.

SnO_2 with various nano- and microstructures, such as nanoparticles, nanorods, nanobelts, hollow microspheres, nanoflowers, nanoperticles, nanowhiskers nanowires and mesoporous structures [8,10–13] has been prepared successfully by different methods. Up to now various methods including molten-salt synthesis [14], chemical precipitation [8], sonochemical [15] carbothermal reduction [16], sol–gel [17], hydrothermal method [13], microwave technique [18], and r.f. sputtering [19], etc. have been developed to fabricate SnO_2 nanostructures.

Xi et al. [8] have reported on the synthesis and characterization of large surface area SnO_2 nanoparticles using ethanol-thermal method with urea and stannic chloride. They have dissolved both precursors in distilled water and heated at 90 °C for 5 h to promote the hydrolysis of $SnCl_4$ and SnO_2 formation. Phani et al. have studied the electrical properties of SnO_2 based liquid petroleum gas (LPG) sensor prepared using tin chloride and ammonia solutions [20]. In order to increase the sensitivity they used noble metal like palladium as a sensitizer. Li et al. [12] studied the fabrication of high-quality rutile SnO_2 nanowires by a vapor phase transport and condensation method assisted by carbothermal reduction. They found that many oxygen vacancies exist in the single-crystalline rutile SnO_2 nanowires and can further influence the photoluminescence (PL) and dielectric property of the nanowires. The PL spectrum only exhibits a wide yellow emission centered at 570 nm and usual near band edge emission is not observed, which is ascribed to a large amount of ionized oxygen vacancies. The dielectric measurements indicate that the dielectric response of the SnO_2 nanowires is significantly enhanced in the low-frequency range. Davar et al. [21] reported the synthesis of SnO_2 nanoparticle using thermal decomposition and characterization of their physicochemical characterization. The SnO_2 nanoparticle powder has been prepared using [bis(2-hydroxyacetophenato)tin(II)],

* Corresponding author. Tel.: +91 231 2609435; fax: +91 231 2691533.
E-mail address: rajpure@yahoo.com (K.Y. Rajpure).

0925-8388/$ – see front matter © 2010 Elsevier B.V. All rights reserved.
doi:10.1016/j.jallcom.2010.06.131

[$Sn(HAP)_2$]; as precursor. Transmission electron microscopy (TEM) analysis was demonstrated that SnO_2 nanoparticle with an average diameter of about 14–22 nm. The novel precursor was thermal treated in solid-state reaction in different temperature, 350, 450, and 550 °C. Kong et al. [22] prepared nanocomposites of SnO_2 and polythiophene (PTP) by the in situ chemical oxidative polymerization method. These nanocomposites were characterized by their physicochemical properties. The composites were used for gas sensing to methanol (MeOH), ethanol (EtOH), acetone, and NOx at different working temperature. It was found that PTP/SnO_2 materials with different PTP mass percent (1%, 5%, 10%, 20% and 30%) could detect NOx with very higher selectivity and sensitivity at much lower working temperature than the reported SnO_2. The sensing mechanism of PTP/SnO_2 nanocomposites to NOx was presumed to be the effects of p–n heterojunction between PTP and SnO_2. Dutta and De [23] synthesized nanostructured tin dioxide (SnO_2) in the form of colloidal solution. Aniline monomer is polymerized in colloidal solution of SnO_2 to prepare inorganic–organic hybrid nanocomposites. Optical band gap increases from 3.74 to 4.23 eV with increase of polyaniline concentration. The observed nonlinear current–voltage characteristics are satisfactorily explained using the Schottky type barriers. The temperature dependence of conductivity reveals three-dimensional Mott's hopping process. Xi et al. [24] studied the synthesis of Al–SnO_2 nanoparticles by a co-precipitation route in water-in-oil microemulsion consisting of water, DBS (surfactant), 1-amyl-alcohol (assistant surfactant) and cyclohexane (oil phase). The results show that the particle size of Al–SnO_2 is below 10 nm, while pure SnO_2 is over 15 nm, which indicates that the introduction of Al can effectively prevent SnO_2 from further growing up in the process of calcination. On the other hand, when the molar ratio of Al to Sn is 1:4 and the calcination temperature is 600 °C, the as-prepared Al–SnO_2 nanoparticles have the lowest particle size in the experiments. In the photocatalytic degradation of phenol, the Al–SnO_2 nanoparticles exhibit better activity than the pure SnO_2 nanoparticles. To control crystallite size they have mixed aluminium silicate as grain growth inhibitor for SnO_2. In a co-precipitation method, the tin oxide is obtained by adding ammonia directly to a solution containing tin cations. This method gives better control over the precipitate particle shape and size due to change of solution concentration and the localized introduction of the ammonia uniformly throughout the solution at the molecular levels.

In this paper we report the successful synthesis and characterization of nanocrystalline high surface area SnO_2 powders using a simple chemical co-precipitation method [25]. The influence of sintering temperature on the structural, FTIR, electrical, morphological, and dielectrical and XPS properties is reported.

2. Experimental

2.1. Preparation of samples

Tin oxide samples were synthesized using a chemical co-precipitation route with AR grade 0.5 M stannic chloride pentahydrate ($SnCl_4{\cdot}5H_2O$). Only double distilled water was used as a solvent. The pH of solution was measured and then adjusted to neutral value by adding aqueous ammonia to preserve the hydroxide phase of tin. The resulted white gelatinous precipitate was filtered using Whatmann filter paper No. 17 and washed thoroughly until traces of Cl have been completely removed. It was further dried in ambient temperature and annealed at different temperatures within 400–1000 °C for 6 h in air atmosphere. These powders were further mixed with polyvinyl alcohol which acts as binder and pressed to form pellets of 15 mm diameter and 2–3 mm thickness using a hydraulic pressure. The elimination of binder from pellets was carried out by heating samples at 300 °C for 1 h.

2.2. Characterization of samples

The samples were characterized by X-ray diffractometer (Philips, Model PW-3710) using Cu Kα radiation (λ = 1.54056 Å) for structural analysis especially to verdict the structure and the crystallite size variation. Fourier Transform Infrared (FTIR) spectra of samples were recorded on Perkin Elmer FTIR Spectrophotometer

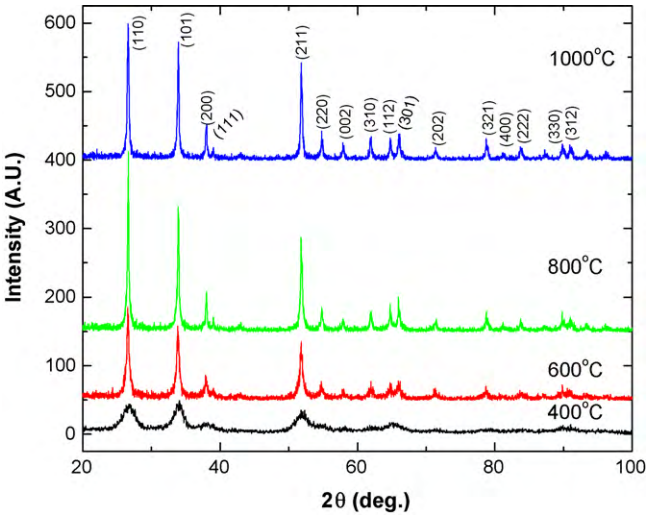

Fig. 1. X-ray diffraction patterns of tin oxide powder sintered at different temperatures.

(4000–450 cm^{-1}) with KBr as compressed slices to understand the nature of bonds present in SnO_2 samples. The surface morphology was investigated using a JEOL JSM-6360 scanning electron microscope (SEM). Resistivity measurements were carried out by two-probe method as a function of temperature from room temperature to 500 °C. For good ohmic contacts silver paste was used. The ac parameters such as capacitance (C_p) and loss tangent of the samples were measured in the frequency range 20 Hz to 1 MHz using LCR meter (HP 4284 A) to estimate the dielectric constant (ε') using the relation [25],

$$\varepsilon' = \frac{C_p t}{\varepsilon_0 A} \quad (1)$$

where C_p is the capacitance of the pellet, t is the thickness of the pellet, A is the area of cross section of the pellet and ε_0 is the permittivity of free space (8.854×10^{-12} F m^{-1}). The ac conductivity (σ_{ac}) of the samples was estimated from the dielectric parameters using the relation [26],

$$\sigma_{ac} = \omega \varepsilon' \varepsilon_0 \tan\delta \quad (2)$$

where ω the angular frequency and $\tan\delta$ is the dissipation factor. For finding the binding energies associated with evolved spectral response and composition analysis the XPS studies were carried out using the model PHI-5400 type X-ray photoelectron spectroscopy with monochromatic Mg Kα (1254 eV) radiation source.

3. Results and discussion

3.1. X-ray diffraction studies

Fig. 1 shows the XRD patterns of the tin oxide samples sintered at different temperatures. The samples are polycrystalline and fit well with the tetragonal crystal structure with space group *P*42/*mnm* (1 3 6). The samples are analyzed by using JCPDS card No. 77-0447. The intensity and number of diffraction peaks are found to be influenced by sintering temperature. The sharpness and peak intensity increases with increase in sintering temperatures due to enhancement in the crystallinity. The decrease in intensity might be due to scattering losses. The samples show strongest growth along the (1 1 0) plane, (1 0 1) and (2 1 1) planes relatively less dominating to (1 1 0) plane, which matches well with the data card 77-0447. The plane (1 1 0) has the highest intensity, which occupies the apical O and Sn atoms, the plane (1 0 1) has the second highest intensity and the plane (2 1 1) has the third highest intensity as observed from XRD patterns. From the calculation of relative intensity ratios of (1 0 1) and (2 1 1) with respect to (1 1 0) of all samples, it is concluded that atomic density is found to be (1 1 0) > (1 0 1) > (2 1 1). No extra phases (such as Sn, SnO, SnO_x, Sn_2O_3 Sn_3O_4, etc.) corresponding to other oxides have been detected. The average lattice parameters of the samples sintered at 400–1000 °C are well agreed with single crystal values confirming the tetragonal phase formation.

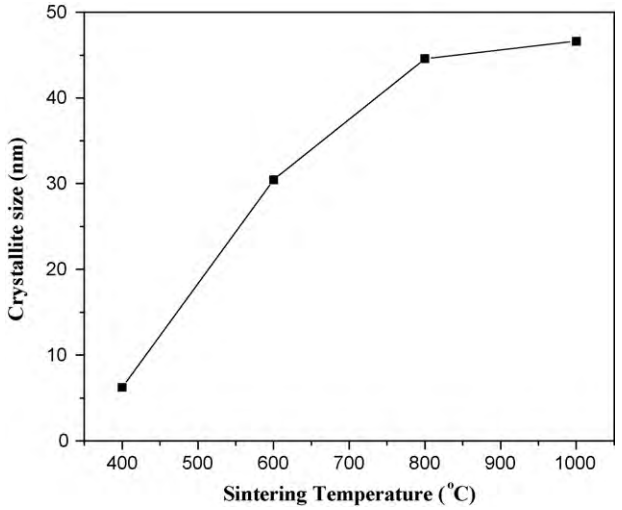

Fig. 2. The variation in crystallite size with sintering temperatures.

The crystallite size of the samples is calculated using the Scherrer's formula,

$$D = \frac{0.9\lambda}{(\beta \cos\theta)} \quad (3)$$

where D is crystallite size, λ is the wavelength of Cu Kα line, β is FWHM in radians (corrected for instrumental broadening) and θ is the Bragg's angle.

The values of average crystallite size of SnO_2 nanoparticles sintered at 400, 600, 800 and 1000 °C are 6, 30, 44 and 46 nm (±5%), respectively (Fig. 2). The occurred crystallite size exactly agreed with values reported by Jain and Lakshmikumar [27]. It is well known that, as sintering temperature increases, crystallite size increases. For gas sensor applications, a smaller particle size is desirable as it provides a greater surface to-bulk-volume ratio resulting in increased adsorption of gases at the sensors surface leading to enhanced sensitivity of the gas sensors. Therefore our samples can be potential candidate for these applications.

3.2. Fourier transform infrared spectroscopy (FTIR)

To understand the nature of the species of the SnO_2 samples sintered at various temperatures, FTIR spectra of samples was recorded. Fig. 3(a–d) shows FTIR spectra of tin oxide samples sintered at various temperatures within 450–4000 cm^{-1}. For 400 °C the various absorption bands located at 673, 1021, 1627, 2923, 3394 cm^{-1} are observed. Broad absorption bands centered at 673 and 1021 cm^{-1} can be assigned to the stretching vibrations of Sn–O and blending vibrations of O–Sn–O bonds, respectively. From Fig. 3 it is observed that the position of Sn–O is centered at 673, 665, 621, and 619 cm^{-1}, for 400 600, 800 and 1000 °C, respectively. The peaks represent the defect or surface vacancies in the crystalline structure of the surface layer. These defects lead to forces on the atoms as a result the bond position changes a little. In other words the bond of Sn–O has little bit drift which indicates relatively less influence on size and shape of unit cell. In terms of surface structural changes, the surface tensile stress decreases as the lattice energy of the surface atoms becomes less and less imposed by the volume atoms, but resulting in the renormalization of their organization. Thus, we confirm that SnO_2 possess the crystalline structure of the tetragonal type, which is in good agreement with the results of XRD. Also, the other characteristic absorption band has appeared with strong shoulder at 1021 cm^{-1} due to both symmetric (ν^1) and

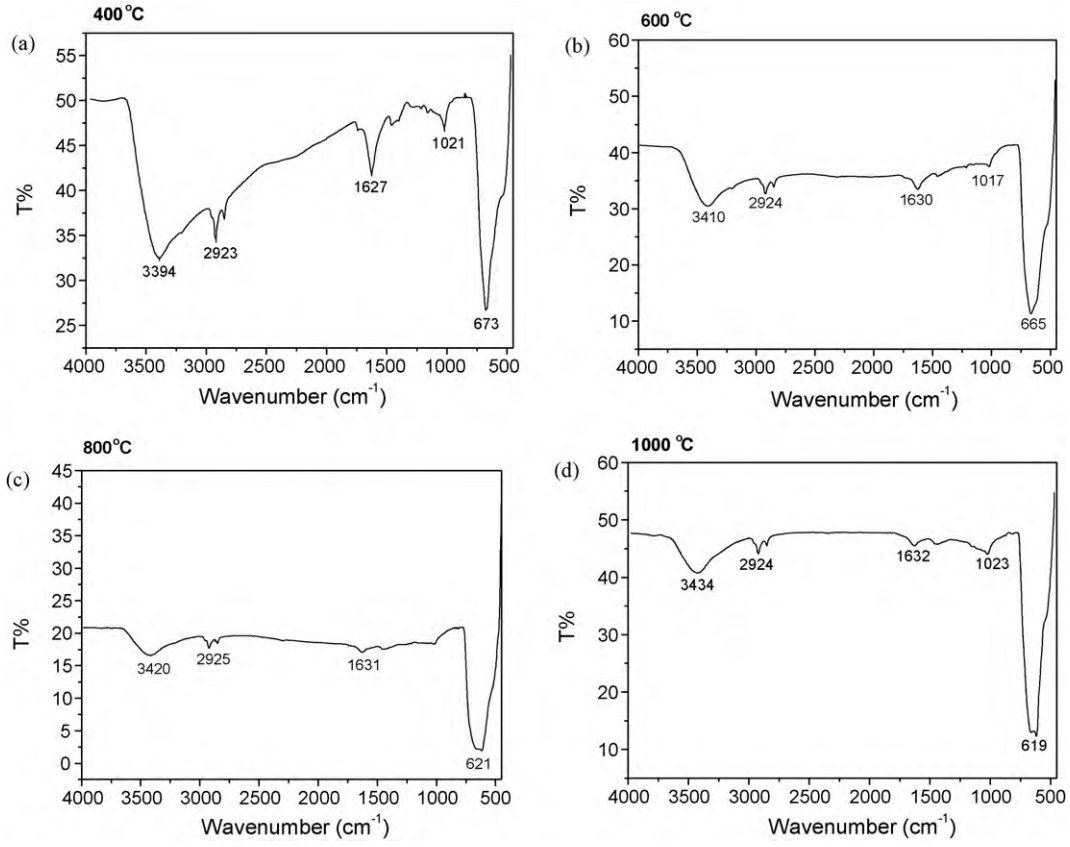

Fig. 3. FTIR spectra of tin oxide samples sintered at different temperatures; (a) 400 °C, (b) 600 °C, (c) 800 °C, (d) 1000 °C.

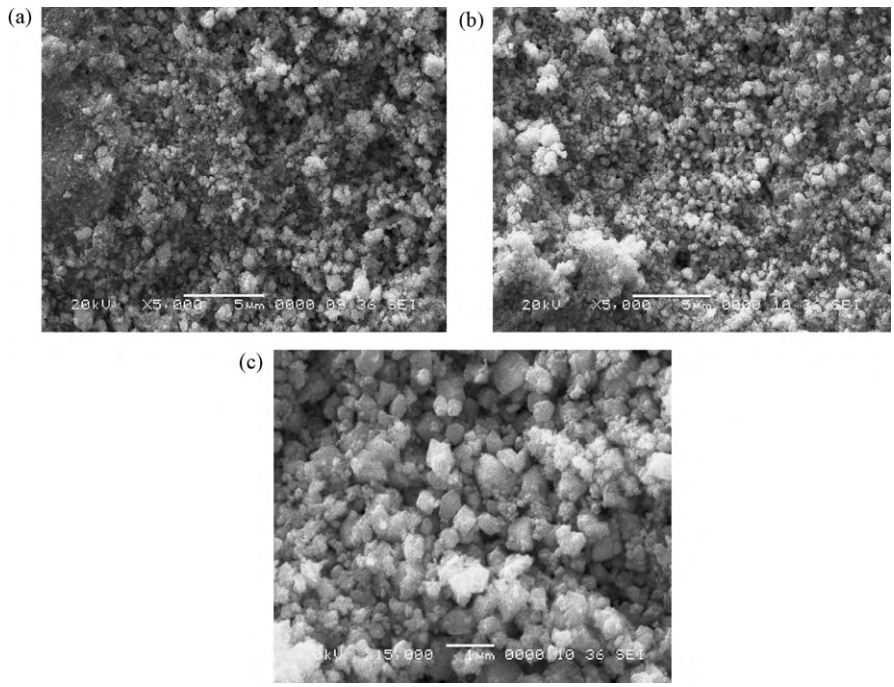

Fig. 4. (a) Morphological image of tin oxide sample sintered at 800 °C with 5000× magnification; (b) morphological image of sample sintered at 1000 °C with 5000× magnification; (c) with 15,000× magnification.

antisymmetric stretching (ν^2) vibrations. The other various absorption bands are attributed to the O–H bond, which come from the physical and chemical adsorbed water in the air [13].

The strengthening of the all bonds decreases as compared to 400 °C temperature except Sn–O and O–Sn–O bonds. As the temperature increases the transmittance decreases up to 800 °C and then increases, probably due to formation of an oxidation of tin dioxide on an oxygen atom of the crystal lattice. Also, for higher temperatures viz. 800 and 1000 °C, we observed severe variation in the shifting of absorption bands. At higher temperatures, a broad absorption band centered at 673 cm^{-1} shift towards 621 and 619 cm^{-1} because of the stretching vibration from Sn–O bond towards blended O–Sn–O bond vibration. For 800 °C absorption bands are weaker than any other temperatures due to reduction in band density absorbed at SnO_2 grain surface. The disappearance of the absorption peak at ≈1021 cm^{-1} indicates that the further polymerization of the Sn–O groups leads to the decrease of the O–H groups linked on the surface of the SnO_2 particles. This trend results in the strengthening the structure through cross-linking, which is strongly correlated with improving physical properties such as hardness and stiffness. Strengthening of O–Sn–O bond increased at 1000 °C due to agglomeration and densely agreement of crystallites occurred during sintering [27].

3.3. Scanning electron microscopy (SEM)

Fig. 4(a) shows morphological image of SnO_2 samples sintered at 800 °C. It reveals randomly arranged irregular sized compact grains with sponge like structure. Some spongy grains are overgrown on the compact sticky grains. Also some deep pits are observed in morphology. So the samples are very much useful in gas sensing application. Fig. 4(b and c) depicts the morphological behavior of samples sintered at 1000 °C with 5000× and 15,000× magnifications, respectively. Highly dense, compact and non-uniformly distributed various sized trapezoidal grains are observed. Spongy cap like grains are overgrown on smaller grains. At higher magnification trapezoidal grains with some pits are clearly seen. From these observations it is seen that grain size of samples depends on temperature. The average grain size increases from 200 to 500 nm with increase in sintering temperature which is analogous to the observed trend of crystallinity.

3.4. Electrical resistivity

Fig. 5 shows the variation of two-probe dc electrical resistivity as a function of inverse temperature. The room temperature dc electrical resistivity of samples sintered at 400, 600, 800, 1000 °C, respectively, has been found to be 5.42×10^2, 5.54×10^2, 9.83×10^2 and 1.42×10^3 Ω cm, respectively. The observed values of resistivity are lower than the single crystal value 4.5×10^6 Ω cm [28] due to formation of oxygen deficient samples (Table 1). The dc resistivity increases with increasing temperature because of the addition

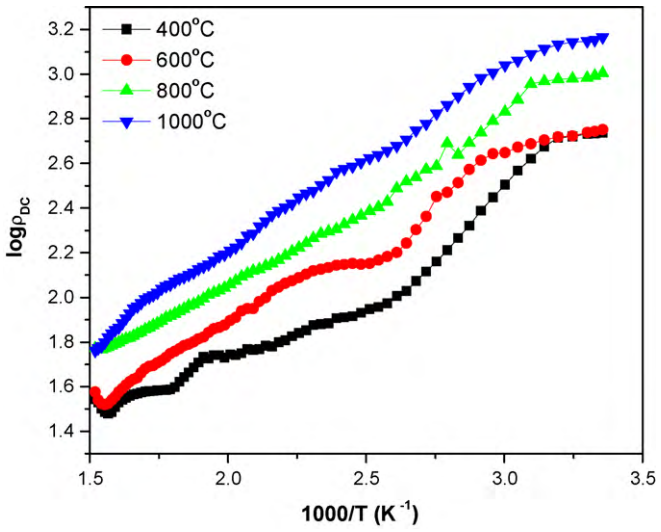

Fig. 5. Variation of dc electrical resistivity with temperature for SnO_2.

Table 1
The compositional analysis of SnO_2 nanoparticles prepared with various sintering temperatures.

Sintering temperature (°C)	The compositional analysis (at.%) from the XPS studies for			
	Sn	O	C	[O]/[Sn]
400	36.12	57.87	6.01	1.6023
600	34.50	58.07	7.43	1.6834
800	34.04	57.61	8.35	1.6920
1000	31.71	57.55	10.74	1.8144

of thermal energy, electron could be set free from O^{2-} ions. When an electron is introduced in the sample it might be associated with cations, which results in an unstable valence state [29]. In the conduction process, the electrical resistivity is known to be affected by grain growth, grain size, inter-grain distribution, pore distribution (porosity) in addition to other blocking effects. The pore distribution being important parameter plays a vital role in deciding the resistivity behavior. In the present case, the increase of electrical resistivity can be related to the decreasing amount of grain-to-grain junction, i.e., increasing the porosity. The porosity is increased with increase in sintering temperature from 400–1000 °C and it varies from 14% to 25%. As we know, when all the grains are connected in three dimensions then the electrical resistivity remains unaffected. Thus, below transition or in the closed pore region, grain resistivity remains approximately constant. But if some of the grains are isolated due to porosity then the resistivity must contain surface resistance component. Further, increase in porosity showing rise in the equivalent surface length is ascribe to resistivity increase.

For studying the defect levels generated in the samples, the activation energy is calculated by using the relation [25],

$$\rho = \rho_0 \ \exp\left(\frac{\Delta E}{kT}\right) \tag{4}$$

where ΔE is the activation energy, ρ is the resistivity at room temperature, k is the Boltzmann constant and ρ_0 is temperature independent constant. The activation energies of samples sintered at 400, 600, 800, and 1000 °C are found to be 0.438, 0.605, 0.62, 0.682 eV, respectively. It is interesting to notice that the activation energy increases for grain relaxation with porosity. As the fraction of isolated grains increases, series resistance due to pore surface trapped in the grains, start to dominate grain or bulk relaxation, resulting into the increase in activation energy. The temperature increases shallow defects levels slightly disperse towards the Fermi level due to significant achievement of stoichiometry.

3.5. Dielectric properties

The room temperature behavior of dielectric properties with frequency is depicted in Fig. 6. It is seen that the dielectric constant (ε') decreases abruptly at lower frequencies and achieve saturation for higher frequencies showing dispersion of dielectric constant at lower frequencies. The decrease in dielectric constant takes place when hoping frequency of electric charge cannot follow the alternations of applied electric field beyond critical frequency. The dielectric constant varies with applied frequency due to charge transport relaxation time. This dielectric dispersion is attributed to the interfacial polarization. Since polarization decreases with increasing frequency and reaches constant values, decrease in dielectric constant with frequency is observed. The large value of dielectric constant ($\approx 10^4$) is associated with space charge polarization and inhomogeneous (viz. impurities, grain structure and pores) dielectric structure. At higher frequencies the losses are reduced and the dipoles contribute to the polarization [30]. The loss factor curve is attributed to domain wall resonance.

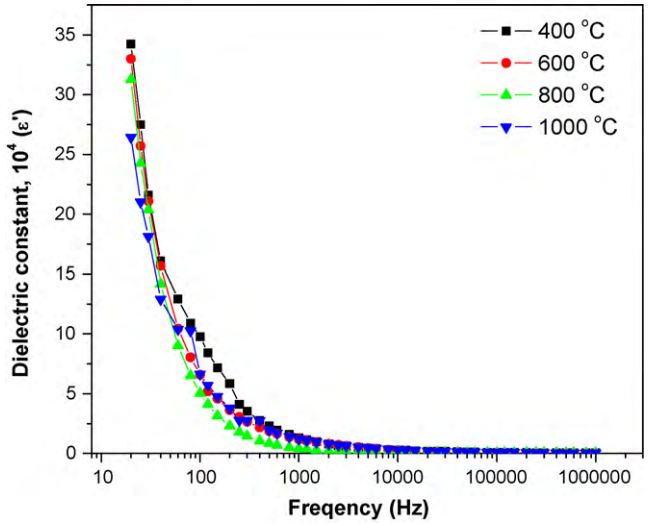

Fig. 6. Room temperature variation of dielectric constant with frequency for SnO_2 powder sintered at different temperatures.

In order to understand the conduction mechanism and the type of polarons responsible for conduction, the variation of ac conductivity as a function of frequency is represented in Fig. 7. In most of the disordered solids, ac conductivity is directly proportional to the frequency. It is also well known that, in large polaron hopping, the ac conductivity decreases with frequency whereas in small polaron hopping it increases with frequency [31]. The electrical conduction mechanism in terms of the electron and polaron hopping model has been discussed by Austin and Mott [32]. In the present case, the plots for $\log \sigma_{ac}$ against $\log \omega$ are linear, indicating that the conduction is due to small polarons. At lower frequencies the grain boundaries are more effective than grains in electrical conduction. In ionic solids the electrical conductivity is due to migration of ions and the ionic transport depends on angular frequency. Thus, the ac conductivity (σ_{ac}) is proportional to the frequency [33]. Relatively higher value of dielectric constant, loss tangent and ac conductivity for sample sintered at 400 °C might be due to observed lower crystallite size.

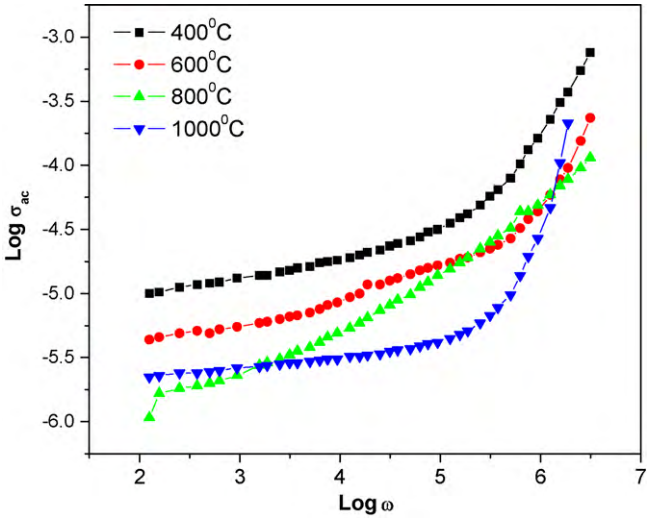

Fig. 7. Variation of ac conductivity with frequency for SnO_2 powder sintered at different temperatures.

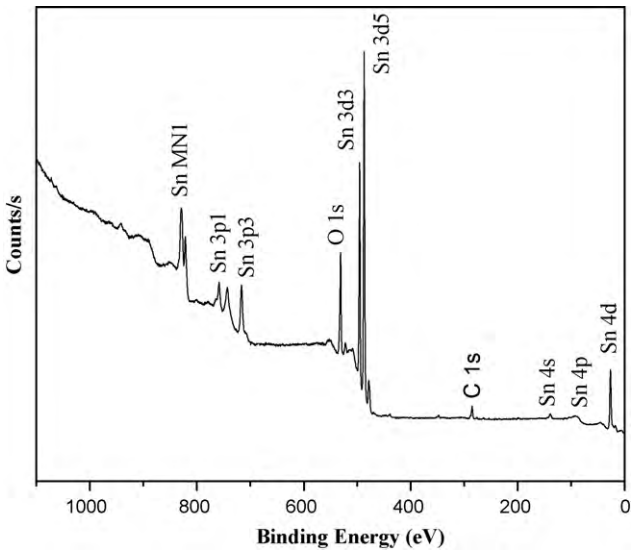

Fig. 8. XPS survey scan spectrum of SnO_2 nano powders sintered at 800 °C.

3.6. XPS analysis

Fig. 8 shows the X-ray photoelectron spectroscopy (XPS) survey scan of SnO_2 sample sintered at 800 °C. Sample contains the Sn, O and traces of C having Sn MN1 auger peak. The presence of C 1s at ≈285 eV is attributed to contamination which resulted from the samples being exposed to air before the XPS measurements [34]. From survey scan spectrum we observed the additional Sn $3p_{1/2}$, $3p_{3/2}$, Sn 4s, Sn 4p, Sn 4d core levels. The narrow scan spectra for tin, oxygen and carbon are shown in Fig. 9(a–c). The spectrum reveals the spin–orbit splitting of the Sn $3d_{5/2}$ ground state and Sn $3d_{3/2}$ excited state core levels of tin in the region of 481.25–491.26 and 491.14–499.46 eV with a better symmetry are assigned to the lattice tin in tin oxide. The separation between the Sn $3d_{5/2}$ and Sn $3d_{3/2}$ level (8.41 eV) is approximately the same as in the standard spectrum of Sn and agrees well with other report [19]. The values correspond to a binding energy of Sn (IV) ion (indexed Standard ESCA Spectra of the Elements and Line Energy Information, Co., USA). It appears that Sn slightly shifts towards lower BE, i.e., to a nearly metallic state, after sintering at higher temperatures (>600 °C). Moreover, the intensity of this lower BE peak is also considerably high. Sintering at higher temperatures shows a transition towards low B.E. regime is found. For the crystals a time-independent concentration is approached, indicating thermodynamic equilibrium between the bulk concentration and the surface layer. The ongoing particle growth processes in the powders derived from the consideration of an effective activation energies. The additional material transport between the powder particles leads to higher effective activation energies in the powders. Therefore, it must be concluded that equilibrium for the powders is reached only at higher temperatures or for longer sintering time than for the single crystals.

The oxygen peaks observed at ≈531, 531.04, 530.7, 530.59 eV for the samples sintered at 400–1000 °C can be attributed to O_2^- state adsorbed at oxygen vacancies respectively due to chemisorbed oxygen in non-stoichiometric oxides. The shift in peak at higher temperature is due to variation in concentration of the oxygen vacancies [35]. The compositional analysis of SnO_2 nanoparticles prepared with various sintering temperatures is shown in the Table 1. The ratio of atomic concentrations (O/Sn) is quantitatively analyzed by calculating the peak areas of the O 1s and Sn $3d_{5/2}$ peaks. The obtained values of 1.60–1.81 deviated from the theoretical one from which it is confirmed that the samples are non-stoichiometric as well as oxygen deficient.

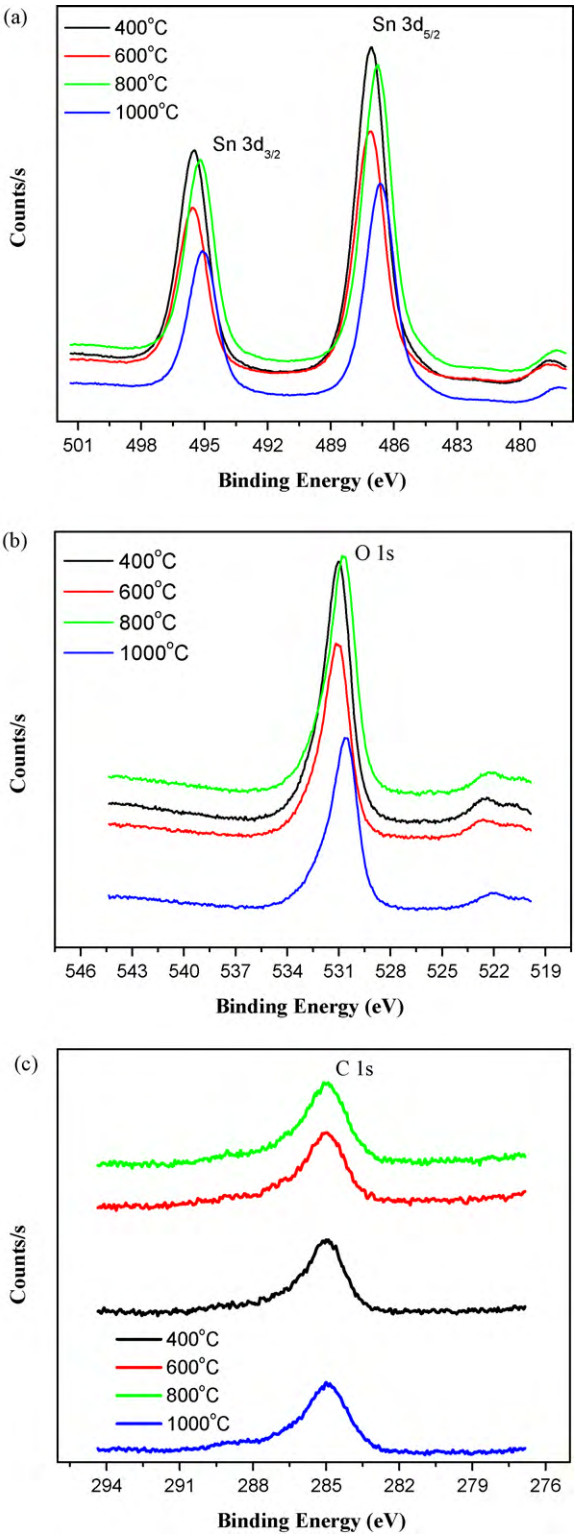

Fig. 9. XPS spectra of the SnO_2 nano powder calcined in air for various temperatures (400–1000 °C) (a) narrow scan of Sn3d; (b) Narrow scan of O 1s; (c) narrow scan of C 1s.

4. Conclusions

The tetragonal tin oxide phase can be synthesized by using chemical co-precipitation technique. Powder sample shows ran-

domly arranged irregular sized compact trapezoidal grains with spongy nature. The nature of species and oxide phase formation is confirmed through FTIR and XPS studies and the various absorption bands such as Sn–O, O–Sn–O and O–H corresponds to 619–673, 1020, 1630, 2923, 3400 cm^{-1}, respectively. The decreasing behavior of dielectric constant with applied frequency is due to charge transport. XPS results show the symmetric spin orbit splitting of Sn $3d_{5/2}$ ground state and Sn $3d_{3/2}$ excited states while O 1s is recognized with O_2^- state.

Acknowledgements

The authors are thankful to University Grants Commission for their support through UGC-DRS-SAP IInd phase programme (2004-2009). The help rendered by R.C. Kambale during electrical measurements is highly acknowledged. AVM wish to thank the Department of Science and Technology (DST), New Delhi for awarding the BOYSCAST Fellowship (File No.SR/BY/P-02/2008) due to which he could provide the characterization facilities and could spent more time during the process of the manuscript.

References

[1] Q. Mao, Z. Ji, L. Zhao, Phys. Status Solidi (B) 247 (2010) 299.
[2] J.J. Berry, D.S. Ginley, P.E. Burrows, Appl. Phys. Lett. 92 (2008) 193304.
[3] A.V. Moholkar, S.M. Pawar, K.Y. Rajpure, C.H. Bhosale, J. Alloys Compd. 455 (2008) 440.
[4] Y.M. Lu, C.P. Hu, J. Alloys Compd. 449 (2008) 389.
[5] K. Park, J.K. Seong, J. Alloys Compd. 464 (2008) 1.
[6] G. Jain, R. Kumar, Opt. Mater. 26 (2004) 27.
[7] S.W. Hwang, S.H. Hyun, J. Power Sources 172 (2007) 451.
[8] L. Xi, D. Qian, X. Tang, C. Chen, Mater. Chem. Phys. 108 (2008) 232.
[9] Y. Zong, Y. Cao, D. Jia, P. Hu, Sens. Actuators B 145 (2010) 84.
[10] H. Huang, O.K. Tan, Y.C. Lee, M.S. Tse, J. Guo, T. White, Nanotechnology 17 (2006) 3668.
[11] P. Andrei, L.L. Fields, J.P. Zheng, Y. Cheng, Sens. Actuators B 128 (2007) 226.
[12] P.G. Li, X. Guo, X.F. Wang, W.H. Tang, J. Alloys Compd. 479 (2009) 74.
[13] D.L. Chen, L. Gao, J. Colloid Interface Sci. 278 (2004) 137.
[14] D. Wang, X.F. Chu, M.L. Gong, Sens. Actuators B 117 (2006) 183.
[15] H.X. Luo, Z. Ying-Ji, W. Shi-Wei, Mater. Chem. Phys. 88 (2004) 421.
[16] S. Thanasanvorakun, P. Mangkorntong, S. Choopun, N. Mangkorntong, Ceram. Int. 34 (2008) 1127.
[17] L. Korosi, S. Papp, V. Meynen, P. Cool, E.F. Vansant, I. Dekany, Colloids Surf. A: Physicochem. Eng. Aspects 268 (2005) 147.
[18] T. Krishnakumar, R. Jayaprakash, N. Pinna, V.N. Singh, B.R. Mehta, A.R. Phani, Mater. Lett. 63 (2009) 242.
[19] H.L. Ma, X.T. Hao, J. Ma, Y.G. Yang, J. Huang, D.H. Zhang, X.G. Xu, Appl. Surf. Sci. 191 (2002) 313.
[20] A.R. Phani, S. Manorama, V.J. Rao, Mater. Chem. Phys. 58 (1999) 101.
[21] F. Davar, M.S. Niasari, Z. Fereshteh, J. Alloys Compd. 496 (2010) 638.
[22] F. Kong, Y. Wang, J. Zhang, H. Xia, B. Zhu, Y. Wang, S. Wang, S. Wu, Mater. Sci. Eng. B 150 (2008) 6.
[23] K. Dutta, S.K. De, Mater. Lett. 61 (2007) 4967.
[24] L. Xi, D. Qian, X. Huang, H. Wang, J. Alloys Compd. 462 (2008) 42.
[25] V.S. Sawant, S.S. Shinde, R.J. Deokate, C.H. Bhosale, B.K. Chougule, K.Y. Rajpure, Appl. Surf. Sci. 255 (2009) 6675.
[26] R.C. Kambale, P.A. Shaikh, C.H. Bhosale, K.Y. Rajpure, Y.D. Kolekar, J. Alloys Compd. 489 (2010) 310.
[27] K. Jain, S.T. Lakshmikumar, J. Surf. Sci. Technol. 21 (2005) 129.
[28] D.R. Lide, CRC Handbook of Chemistry and Physics, 79th ed., CRC Press, 1998, 12–102.
[29] R. Rai, N.C. Soni, S. Sharma, R.N.P. Choudhary, in: A.P. Tandon (Ed.), Ferroelectrics and Dielectrics, Allied Publishers Pvt. Ltd., New Delhi, 2004, p. 177.
[30] D.C. Agrawal, Asian J. Phys. 6 (1997) 108.
[31] R.C. Kambale, P.A. Shaikh, C.H. Bhosale, K.Y. Rajpure, Y.D. Kolekar, Smart Mater. Struct. 18 (2009) 115028.
[32] I.G. Austin, N.F. Mott, Adv. Phys. 18 (1996) 411.
[33] K.K. Patankar, S.S. Joshi, B.K. Chougule, Phys. Lett. A 346 (2005) 337.
[34] D. Kim, S. Kim, Surf. Coat. Technol. 176 (2003) 23.
[35] T. Szörenyi, L.D. Laude, I. Bertoti, Z. Kantor, Z. Geretovszky, J. Appl. Phys. 78 (1995) 6211.